# EFFECTS OF JET EXHAUST ON ENGINE INLET DISTORTION DURING CARRIER-BASED AIRCRAFT TAKEOFF

***Xiaoxi YANG [1], Baokuan LI[1,*], Yang NIE[1], Zhibo REN[2]***

[1] Department of Engineering Thermophysics, Northeastern University, Shenyang, China

[2] Shenyang Aeroengine Research Institute, Aero Engine Corporation of China, Shenyang, China

[*] Corresponding author; E-mail: libk@mail.neu.edu.cn

*During carrier-based aircraft takeoff, the jet exhaust interacts with the jet blast deflector (JBD), generating backflow that affects the intake conditions of the aircraft engine and increases the risk of engine surge and failure. To investigate the characteristics of the jet exhaust backflow, a flow field study was conducted for the carrier-aircraft system during the takeoff phase. A Delayed Detached-Eddy Simulation (DDES) turbulence model coupling the exhaust concentration and temperature fields was developed to examine the temperature and total pressure distortion at the engine aerodynamic interface plane (AIP) under the influence of carrier wake disturbances. The effects of wind direction and deflector angle on inlet distortions were quantified. The results indicate that the maximum temperature distortion at the engine inlet occurs under headwind navigation conditions. Ingestion of high-temperature exhaust reduces the average gas density, leading to a 23.1% reduction in mass flow rate and an 8.6% decrease in oxygen concentration. As the wind direction angle increases, the exhaust backflow deflects, resulting in reduced temperature distortion at the engine inlet and decreased fluctuations in pressure distortion amplitude.*

Key words*: high temperature flow, aero engine, temperature distortion, jet exhaust, Numerical simulation, DDES*

## 1. Introduction

During the takeoff of carrier-based aircraft, engines operate at maximum power to achieve maximal acceleration, resulting in the expulsion of high-temperature, high-velocity exhaust streams. To protect personnel and equipment on the deck, jet blast deflectors (JBD) are installed behind the aircraft to direct the exhaust into the air [1, 2]. However, the interaction between the exhaust and the deflector leads to the formation of a recirculation zone. This backflow, once ingested by the engine's air intake, destabilizes the intake conditions, causing inlet temperature distortions that diminish engine stability and efficiency. In extreme cases, this can induce engine surge or even complete engine failure[3].

Several studies have demonstrated that inlet distortion and separation behavior significantly affect the performance and operational stability of gas induction system through both experimental measurements and numerical simulations [4-10]. Zhang et al. [11] found that blade stall occurs due to flow separation in distorted regions. Coschignano et al. [12] identified that a thicker intake boundary layer in rear-mounted or semi-embedded engine configurations causes total pressure distortion. Zhang

et al. [13] showed that multiple distortion zones reduce compressor performance. Vagnoli et al. [14] revealed that curved duct-induced distortion contributes to rotating stall caused by tip vortices. Rademakers et al. [15] found that total pressure distortion impacts compressor stability more than dual swirl distortion. Triantafyllou et al. [16] assessed distortion levels in the fighter, identifying critical flight conditions where distortion indices peak. However, these studies highlight the critical role of inlet distortion in engine stability, often overlooked in the context of carrier-based aircraft takeoff conditions. Engines operating under off-design conditions are impacted by inlet flow distortion, which reduces stability and efficiency [17]. The takeoff phase of carrier-based aircraft is an unconventional operating condition. During the phase, the carrier typically sails at 30 knots to enable the aircraft to achieve its maximum airspeed. Airflow over deck and island structures causes flow separation and recirculation. This unconventional condition, coupled with exhaust gas backflow, complicates jet plume prediction and further degrades intake quality [18]. The exhaust jet involves complex phenomena including shear flow and mixing. Numerical simulation serves as a critical methodology for high-speed flow studies [19, 20].

Various numerical studies have been conducted to predict the airwake of naval ships [21-26]. However, numerical simulation of ship airwake is still a big challenge due to the turbulent, complicated, unsteady, and separated behavior. Zhang et al. [27] predicted an asymmetric flow distribution above the helicopter deck at the stern of the hull. Watson et al. [28] employed the (Delayed Detached-Eddy Simulation) DDES model to simulate the carrier's airwake. During navigation, the starboard wind can cause flow separation around the dual-island structure of the carrier. Shukla et al. [29] used Reynolds-Averaged Navier-Stokes (RANS) shear-stress transport (SST) $k$-$\omega$ simulations to analyze carrier airflow, revealing that crosswinds significantly contribute to adverse aerodynamic conditions above the flight deck. Forrest et al. [30] and Shukla et al. [31] compared different turbulence models and demonstrated that DES model can accurately predict the flow around a hull. The model can resolve the dominant frequency range in the airwake and the details of the flow field. Zamiri et al. [32] used the DDES model to indicate that larger wind direction angles significantly increase pressure fluctuations and unsteadiness above the ship's deck.

Studies reveal that hull-induced airflow disturbances during navigation cause flow separation and recirculation, with high gradients and rapid fluctuations. Few, however, examine jet exhaust backflow under the hull's airwake. Wang et al. [33] reported that exhaust ingestion with the deflector significantly increases temperature distortion at the aerodynamic interface plane (AIP).

Although studies on both engine inlet distortion and ship's external flow field have been conducted, most studies fail to couple the two aspects in analysis, and current research still predominantly relies on RANS. Previous studies have overlooked intake gas composition, with variation of $CO_2$, $H_2O$ and $O_2$ degrading combustion efficiency and causing instability. Establishing the relationship between temperature distortion and intake gas composition can enable improved engine condition monitoring and control.

To address these gaps, DDES model is employed to comprehensively investigate the dynamic variation of temperature distortion at the AIP section under the airwake during takeoff phase, coupled with a species transport model to quantify gas concentration variations. The numerical approach is validated against PIV-measured supersonic impinging jet data. This framework links temperature distortion, gas composition, and pressure fluctuations to explain engine instability mechanisms during takeoff.

## 2. Numerical model

### 2.1. Governing equations

The engine exhaust jet involves high-temperature, high-velocity compressible flow interacting with lower-speed flow, resulting in shear flow behavior between the two. When the exhaust jet impacts the deflector, it creates a complex turbulent pulsating flow field, accompanied by mass transfer between the various exhaust components and the surrounding air. This study employs a DDES approach [34, 35], which solves the Favre-averaged Navier-Stokes (FANS) equations to account for the density fluctuations in the compressible flow. The model combines SST *k*-$\omega$ model near walls with Large Eddy Simulation (LES) for free shear flows. The improved DDES formulation, with a generalized relationship between grid scale and wall distance, ensures smooth transitions and is better suited for complex geometries like ships and aircraft. The flow medium is modeled as an ideal gas. The simulations were performed using Siemens Star-CCM+ 2023.1.1 with user-defined field functions to calculate the parameters at the AIP. The governing equations are as follows:

$$\frac{\partial(\bar{\rho}\,k)}{\partial t}+\frac{\partial\left(\bar{\rho}\,\tilde{u}_j k\right)}{\partial x_j}=P_k-\bar{\rho}\,\frac{k^{3/2}}{l_{DDES}}+\frac{\partial}{\partial x_j}\left[\left(\mu+\frac{\mu_t}{\sigma_k}\right)\frac{\partial k}{\partial x_j}\right] \tag{1}$$

$$\frac{\partial(\bar{\rho}\omega)}{\partial t}+\frac{\partial\left(\bar{\rho}\,\tilde{u}_j\omega\right)}{\partial x_j}=\frac{\partial}{\partial x_j}\left[\left(\mu+\frac{\mu_t}{\sigma_\omega}\right)\frac{\partial\omega}{\partial x_j}\right]+2(1-F_1)\frac{\sigma_{\omega 2}\bar{\rho}}{\omega}\frac{\partial k}{\partial x_j}\frac{\partial\omega}{\partial x_j}+\alpha\frac{\bar{\rho}}{\mu_t}P_k-\beta\bar{\rho}\omega^2 \tag{2}$$

where $k$ is the turbulent kinetic energy, $\omega$ is the specific dissipation rate. $t$ is real time, $\bar{\rho}$ is the the Reynolds-averaged density, $\tilde{u}_j$ denotes a component of the Favre-averaged velocity vector., $x_j$ is the spatial coordinate component, $\mu$ is the dynamic viscosity, $\mu_t$ is the turbulent viscosity, $\sigma_k$ and $\sigma_\varepsilon$ are model constants used to control unsteadiness, $P_k$ is the production of turbulent kinetic energy, $l_{DDES}$ is the DDES model length scale, $F_1$ is blended function, $\alpha$ is production coefficient for $\omega$, $\beta$ *is* destruction coefficient for $\omega$.

After the combustion of hydrocarbon fuels in the engine, the exhaust gas consists of nitrogen, carbon dioxide, water, and a small amount of oxygen. The interaction between the exhaust and the air results in multi-species convection and diffusion. The species transport equation is as follows:

$$\frac{\partial}{\partial t}(\rho Y_i)+\nabla\cdot(\rho\vec{v}Y_i)=-\nabla\cdot\vec{J}_i \tag{3}$$

where $Y_i$ is the mass fraction of the species and $\vec{J}_i$ is the diffusion flux. The radiative heat transfer of the high-temperature gas from the engine exhaust is modeled using the Discrete Ordinates (DO) method.

$$\nabla\cdot(I_r(\vec{r},\vec{s})\vec{s})+(a+\sigma_s)I_r(\vec{r},\vec{s}')=an^2\frac{\sigma T^4}{\pi}+\frac{\sigma_s}{4\pi}\int_0^{4\pi}I_r(\vec{r},\vec{s}')\Phi(\vec{s},\vec{s}')\mathrm{d}\Omega' \tag{4}$$

where $I_r$ is the radiation intensity, which is a function of the position vector $\vec{s}$ and the direction vector $\vec{r}$ . $\vec{s}'$ is the scattering direction vector, $a$ is the absorptivity, $n$ is the refractive index, $\sigma_s$ is the scattering coefficient, and $\sigma$ is the Stefan-Boltzmann constant $5.67\times10^8$ W/(m$^2$·K$^4$), $\Phi$ represents the phase and $\Omega'$ is the solid angle.

### 2.2. Physical models and boundary conditions

The geometric models used in this study feature an aircraft carrier with a ski-jump deck structure and a heavy carrier-based aircraft. The aircraft is positioned at the takeoff position in the center of the deck. The position of the carrier and the aircraft, main model dimensions and boundary conditions, are shown in Fig. 1. The boundary conditions outside the domain represent atmospheric conditions, with the bottom surface as the water, which moves at the same velocity as the air. The wind direction is varied by adjusting the combination of the front and side boundaries. Fig. 1(b) shows the geometric model and

key dimensions of the aircraft and the JBD. In this study, small structures on the carrier were simplified, but the ski-jump deck, island, and the deflector at the takeoff position were retained. The carrier-based aircraft retains the inlet duct and the auxiliary intake grilles. The significant size differences between these structures and aircraft carrier model pose considerable challenges for grid generation. Fig. 1(c) illustrates schematic diagram of the engine cross-section. The flow passes through the inlet duct, the engine core, and the exhaust nozzle. Fig. 1(d) shows the detailed geometry of the inlet duct and the auxiliary intake grille. The AIP section, serving as a critical reference plane for evaluating intake distortion and engine performance matching, is defined as the interface between the air duct outlet and engine inlet [36]. The AIP section was positioned 0.1 m upstream of the engine inlet to enable accurate monitoring of pressure and temperature distributions prior to the compressor.

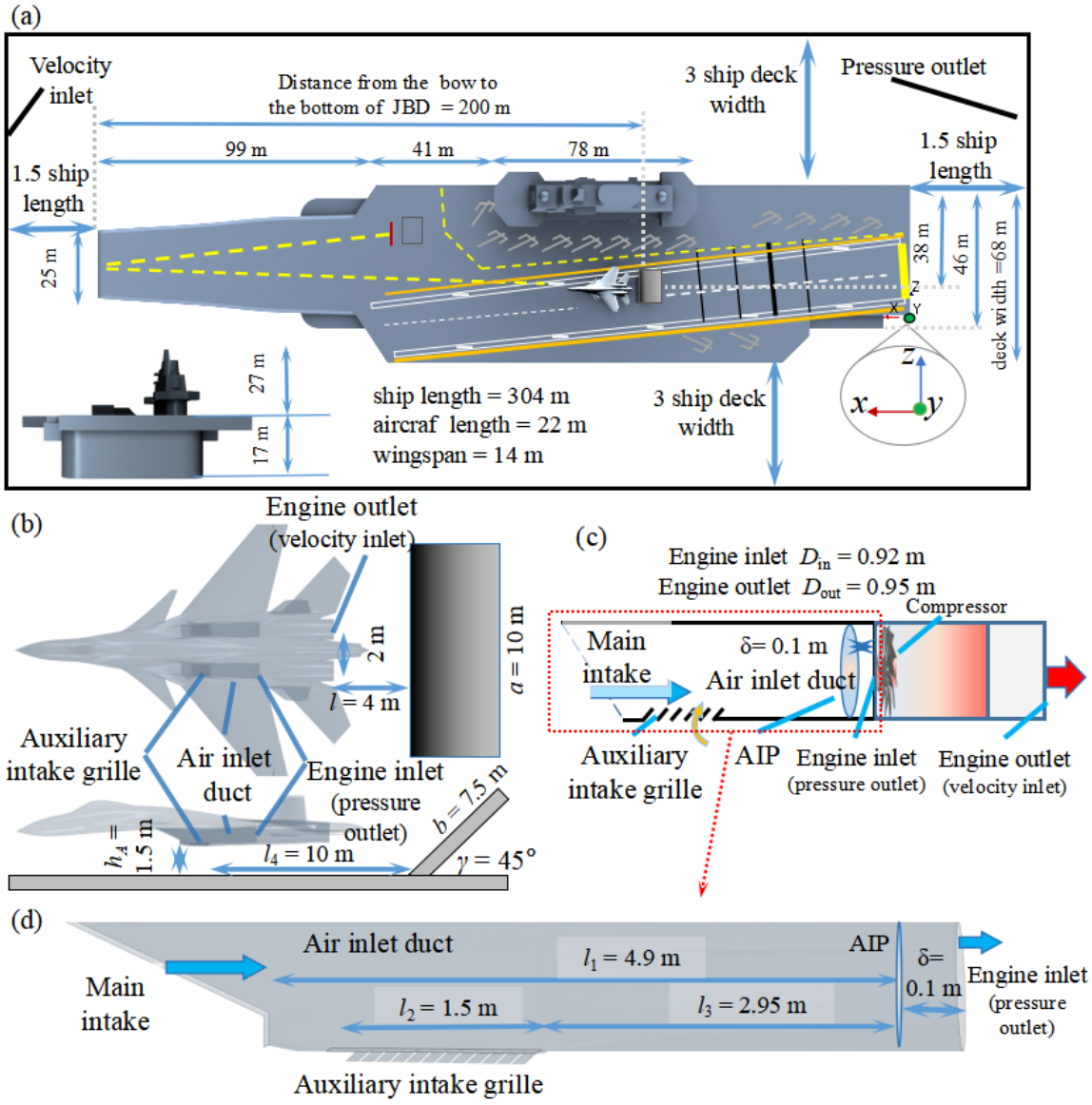


**Figure 1. Geometry models and boundary condition: (a) geometry models, key parameters and computational domain boundary conditions (b) the aircraft and JBD, (c) the engine, (d) the air inlet duct**

This study adopts the AL-31F series engine as the reference. The computational model neglects the compressor and the internal fuel combustion process of the engine. Based on the engine boundary conditions from the reference [33], the exhaust outlet of the engine operates as a velocity outlet, with an exit flow rate of 120 kg/s and a temperature of 1900 K. The engine inlet boundary condition is specified

as a pressure outlet with −25 kPa gauge pressure, maintaining 10% lower mass flow than the exhaust outlet. The ambient temperature is 293 K. Given the complex composition of aviation kerosene, this study assumes the fuel to be pure octane, with an excess air ratio of 1.2. The component mole fractions at the engine outlet are calculated based on the principle of component conservation, as listed in Table 1.

**Table 1. Engine exhaust composition parameters**

| Component | $N_2$ | $CO_2$ | $H_2O$ | $O_2$ |
|---|---|---|---|---|
| Volume fraction | 0.76 | 0.10 | 0.11 | 0.03 |

Typically, when the carrier-based aircraft takes off, the aircraft carrier sails into the wind at a speed of 30 knots (15.4 m/s), enabling the aircraft to achieve maximum airspeed. In the simulation, the relative wind speed is used in place of the vessel's speed. The wind speed is maintained at 15.4 m/s when varying the wind direction angle. Under windy conditions, the airflow through the entire computational domain is calculated, while the engine inlet and outlet remain inactivated. The time step for this stage is 0.01 s. After the carrier's airwake has fully developed, the engine intake and exhaust boundaries are activated. The time step for this stage is $10^{-4}$ s. It is assumed that the aircraft leaves the takeoff position after 3 seconds, at which point the simulation is terminated.

### 2.3. Mesh generation and independence validation

The mesh division for the computational domain and geometric surfaces is illustrated in Fig. 2. Polyhedral mesh is applied throughout the computational domain. Polyhedral grids exhibit excellent geometric adaptability with an average of 14 cell faces. Applying polyhedral grids to the geometric complexity of aircraft carriers and airplanes significantly improves computational efficiency and solution stability. The boundary layer on the surfaces of the aircraft carrier and aircraft consists of 12 layers of mesh, with the first layer having a thickness of 0.01 m and a growth rate of 1.2. Inside the aircraft's intake duct, the first layer mesh thickness is set to 0.001 m. Due to the high velocity gradients in the intake duct and engine exhaust plume, local mesh refinement is applied in these areas by controlling the wall mesh size and growth rate around the intake and auxiliary air intake regions. Airwake refinement is also used along the engine exhaust line and in the region near the JBD to manage mesh size in the flow region.

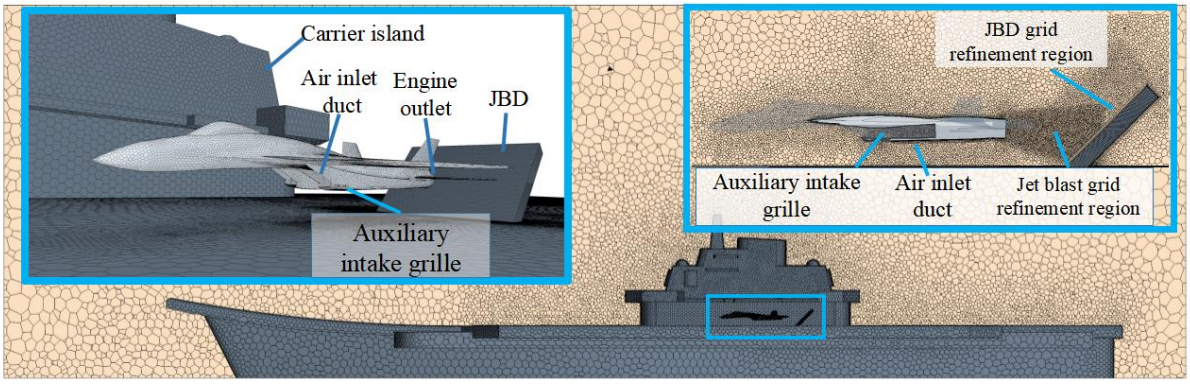


**Figure 2. Mesh of aircraft carrier and aircraft**

Grid independence was confirmed by refining the mesh from 10 million to 27 million cells in the computational domain. Wake refinement method was applied to the jet region (labeled "Jet blast grid refinement region" in the upper-right inset of Fig. 2), where the special mesh refinement method locally

enhanced resolution in high-velocity and high-temperature-gradient zones. The cell count in this region rose from 0.4 million to 1.2 million to better resolve shear layer dynamics and mixing phenomena. Fig. 3 compares temperature and Mach number distributions along the centerline for different mesh resolutions.

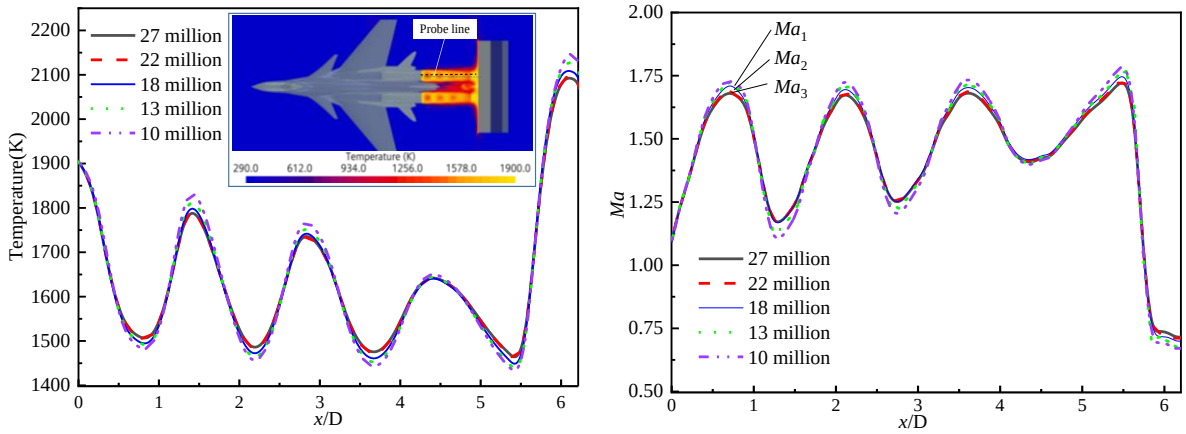


(a) Temperature (b) *Ma*

**Figure 3. Mesh independence validation**

Grid convergence analysis was performed using maximum differences (extrema) along the three finest grids from grid independence validation, with locations in Fig. 3(b) and values in Table 2. The grid refinement ratio r is approximately 1.1. According to the Richardson extrapolation formula:

**Table 2 Grid convergence metrics**

| Grid number | Mach number | Value |
|---|---|---|
| 18 million | $Ma_1$ | 1. 7031 |
| 22 million | $Ma_2$ | 1. 6991 |
| 27 million | $Ma_3$ | 1. 6959 |

$$p = \frac{\ln\left(\frac{Ma_1 - Ma_2}{Ma_2 - Ma_3}\right)}{\ln(r)} = 2.3 \tag{5}$$

$$Ma_{ext} = \frac{r^p Ma_3 - Ma_2}{r^p - 1} = 1.6831 \tag{6}$$

$$\varepsilon = \left|\frac{Ma_{ext} - Ma_2}{Ma_{ext}}\right| \times 100\% = 0.9\% \tag{7}$$

where $p$ denotes the order of convergence, and $Ma_{ext}$ represents the Richardson extrapolated value at the asymptotic grid-independent limit. The calculated convergence order $p$ = 2.3 with a relative error of $\varepsilon$ = 0.9% (relative to the extrapolated value) demonstrates reliable grid independence verification. Results demonstrate asymptotic convergence from 22 million grids to the grid-independent solution. Therefore, 22 million grids were selected for subsequent simulations.

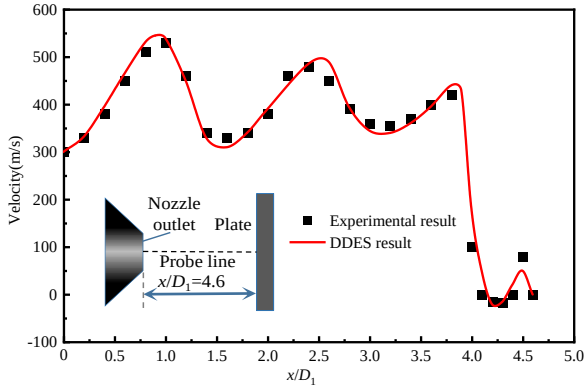


**Figure 4. Verification of the numerical model**

## 2.4. Verification of the numerical model

To ensure the accuracy of the numerical model used in this study for calculating the engine jet flow, the DDES result were compared with experimental data from high-speed jet impact tests on a flat plate [37]. The experimental subject closely resembles the engine jet flow impacting the deflector in this study. Therefore, it serves as a valid basis for verification. $D_1$ represents the diameter of the nozzle exit and $x$ is the distance from the nozzle exit. The flat plate is located at a distance of $x/D_1$=4.6, with a nozzle pressure drop

ratio (NPR) of 4.03. Fig. 4 shows that the numerically simulated velocity profile along the jet centerline agrees well with the experimental data. This consistency validates the accuracy of the numerical calculation model.

### 2.5. Parameter definitions and calculations

The total pressure recovery coefficient is defined as the ratio of the total pressure at the AIP to the undisturbed total pressure before the intake, calculated according to Eq. (8):

$$\sigma_{\mathrm{TPR}}(\bar{r},\theta)=\frac{P_{t1}(\bar{r},\theta)}{P_{t0}} \tag{8}$$

where $P_{t0}$ is the undisturbed total pressure of the airflow before the intake, measured in Pa.

The circumferential distortion index represents the relative difference between the average total pressure recovery coefficient at the AIP and the average total pressure recovery coefficient within the low-pressure sector, as shown in Fig. 5. In this study, it is referred to as the total pressure distortion and is calculated according to Eq. (9):

$$\Delta\bar{\sigma}_0=1-\frac{\sigma_0}{\sigma_{\mathrm{av}}} \tag{9}$$

where $\sigma_0$ is the average total pressure recovery coefficient within the low-pressure zone, which represents the ratio of the area average total pressure in the low-pressure zone to the undisturbed total pressure of the airflow upstream of the intake. The value of $\sigma_0$ is calculated according to Eq. (10):

$$\sigma_0=\frac{1}{\theta_2-\theta_1}\int_{\theta_1}^{\theta_2}\sigma_{\mathrm{r,av}}(\theta)\,\mathrm{d}\theta \tag{10}$$

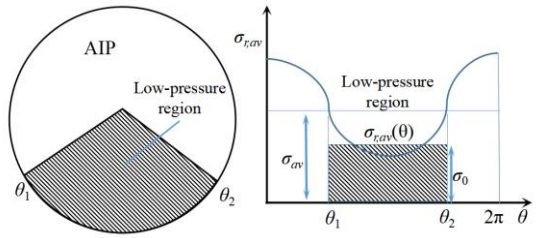


**Figure 5. Schematic diagram of total pressure distortion at AIP**

where $\theta_1$ and $\theta_2$ represent the start and end angles of the low-pressure sector, respectively.

The total temperature distortion intensity is defined as the ratio of the area averaged temperature rise to the reference temperature, expressed as follows:

$$\Delta T_{\mathrm{AIP}}=\frac{T_{\mathrm{AIP}}-T_0}{T_0} \tag{11}$$

where $T_{\mathrm{AIP}}$ is the area average temperature at AIP, and $T_0$ is the total temperature of the free stream, serving as the reference temperature, measured in K.

## 3. Results and Discussion

### 3.1. Effect of exhaust jet on AIP characteristics

This subsection analyzes the exhaust plume development, AIP flow structures, and the transient coupling between temperature distortion, gas composition, and intake flow rate. Fig. 6 shows the spatial distribution of the engine exhaust flow temperature under headwind conditions. The result are consistent with the numerical simulation results in reference [33]. The figure shows that most of the exhaust is directed upward into the air after impacting the deflector. The exhaust gas is driven by the external flow field, developing towards the aft side, and forming a recirculation zone behind the deflector. A portion of the exhaust gas accumulates, and rapidly reflects towards the aircraft's intake area.

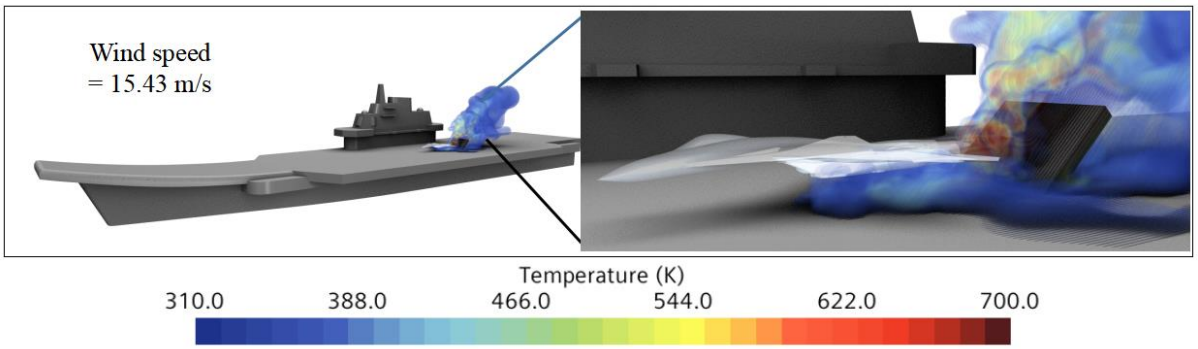


**Figure 6. Spatial temperature field of aircraft exhaust with JBD activated**

Fig. 7 illustrates the flow field distribution at the AIP after the engine intakes ingest high-temperature exhaust under headwind condition. The external environments lead to an asymmetrical flow field distribution across the two engine intake ducts. Due to the characteristics of the air inlet duct structure and the auxiliary intake grilles at the bottom, the external airflow drawn into the intake ducts forms a high-speed region in the upper part of the ducts. A low-speed region forms at the bottom of the AIP, while the upper half features a crescent-shaped a high-speed region. The total pressure distribution at the AIP aligns with the velocity distribution. The tangential velocity distribution reveals a pair of counter-rotating swirls directed upward at the center of the AIP. Since the exhaust backflow initially reaches the auxiliary intake grilles, the majority of the exhaust gas is ingested into the intake duct through these grilles. The ingestion of high-temperature gas results in temperature distribution differences at the AIP, with high-temperature zones primarily concentrated in the middle and lower parts of the AIP. The non-uniform and transient distributions of total pressure, velocity, and temperature at the AIP adversely affect the stability and efficiency of the compressor blades.

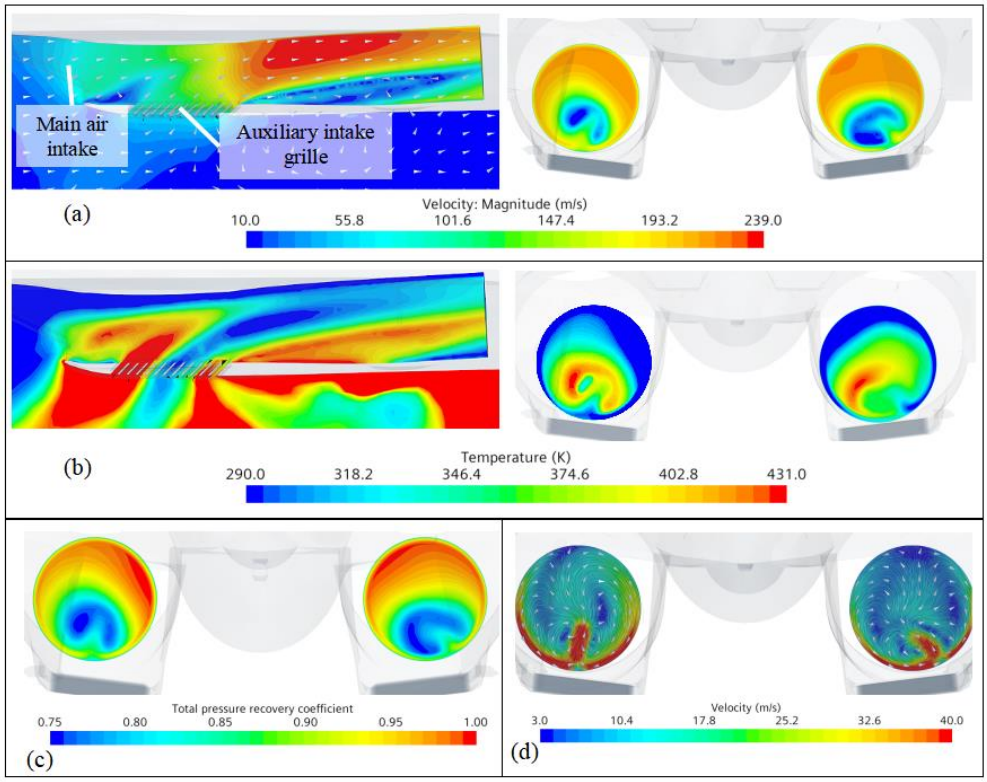


**Figure 7. Flow field at AIP under headwind condition, (a) velocity, (b) temperature, (c) total pressure recovery coefficient, (d) tangential velocity**

Fig. 8 illustrates the dynamic relationships between temperature distortion, gas component concentration, and intake flow rate at the AIP of the intake duct under headwind. Before the intake of exhaust gas, the gas undergoes expansion, resulting in a total temperature lower than the reference temperature, while the inlet flow rate remains stable. After 0.8 seconds of engine activation, the engine begins to intake exhaust gas. The temperature distortion at the AIP rapidly increases, reaching a maximum of 0.49. Concurrently, the concentrations of $CO_2$ and $H_2O$ also rise, while the oxygen concentration decreases by 8.6%, and flow rate decreases by 23.1%. There is a strong positive correlation between total temperature distortion and $CO_2$ and $H_2O$ mole fraction, and a strong negative correlation with the $O_2$ mole fraction and flow rate. Therefore, monitoring total temperature distortion can provide insights into the values of other variables.

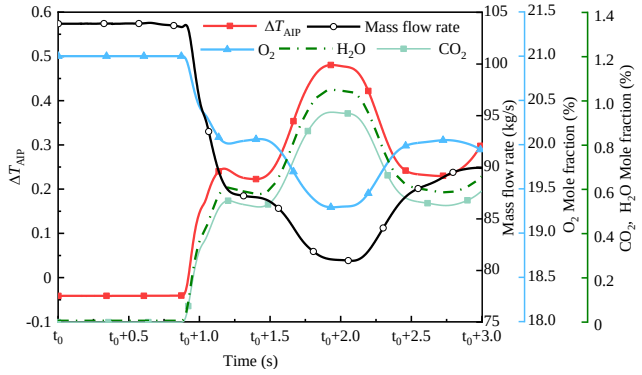


**Figure 8. Temperature distortion, gas composition, and flow rate during exhaust ingestion under headwind conditions**

As temperature distortion increases, the density of the intake gas inevitably decreases, leading to reduced efficiency of the compressor blades. The decline in airflow rate and oxygen concentration, along with the rise in $CO_2$ and $H_2O$, results in incomplete fuel combustion, thereby decreasing combustion efficiency within the engine's combustion chamber. These adverse operating conditions for the engine occur simultaneously, causing the performance of the compressor components and combustion conditions to deteriorate with ingestion of exhaust jet.

### 3.2. Effect of wind direction

This subsection evaluates the effects of wind direction on the exhaust path, asymmetric distortion, and the statistical characteristics of temperature and pressure distortion. Fig. 9 depicts the jet exhaust flow field subject to hull airwake disturbances under different wind direction, coloured by velocity magnitude. In no-wind condition, the recirculating exhaust flows primarily along the aircraft's centerline. Since the backflow is driven by accumulated gas, the flow tends to be unstable, leading to oscillations during the recirculation process. The reflected exhaust flow deflects when encountering the headwind.

Due to the obstruction at the ship's edges, flow separation occurs, leading to recirculation zones around the island and deck edges. With a starboard wind, a recirculation zone forms to the left of the island, while a portside wind creates a recirculation zone along the left deck edge. As the wind angle increases, the influence of the recirculation zone expands. The direction of the high-temperature core of the exhaust backflow is no longer a simple downwind deflection but shifts according to the direction of the recirculation zone. This is most evident at a wind direction angle of 45°, where the high-speed zone deflects toward the upwind side.

Fig. 10 illustrates the temperature and streamlines at a plane located 1.0 m above the deck. It reflects the extent and direction of the high-temperature gas flow. Under no wind condition, the high-temperature zone is concentrated directly beneath the aircraft's intake and continues to extend forward. Some exhaust gas developed laterally towards the sides of the deflector, while no high-temperature zone is present on the leeward side of the deflector. In windy conditions, the

high-temperature region of the exhaust experiences deflection during backflow, with the high-temperature zone passing directly beneath the auxiliary intake. When the wind direction angle is no more than 22.5°, most of the high-temperature exhaust flows beneath the fuselage and near the auxiliary intake of both engines, creating a secondary vortex in the recirculation area. This indicates that the exhaust gathers in this region, leading to the engine ingesting substantial amounts of high-temperature gas. As the wind direction angle increases to 45°, the deflection of the exhaust recirculation intensifies. Before reaching the auxiliary intake grille, it shifts outside the influence range of the intake, resulting in only a small portion of the exhaust being drawn.

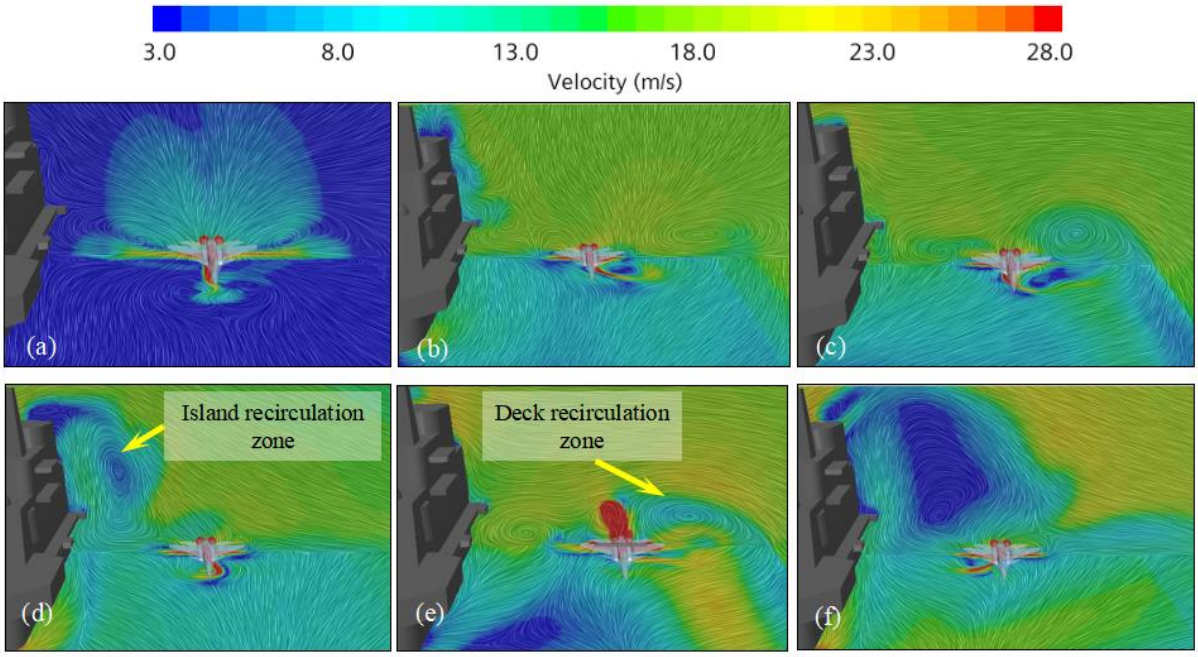


**Figure 9. Exhaust flow field of carrier-based aircraft under different wind direction: (a)no wind, (b)headwind, (c)left 22.5°, (d)right 22.5°, (e)left 45°, (f)right 45°**

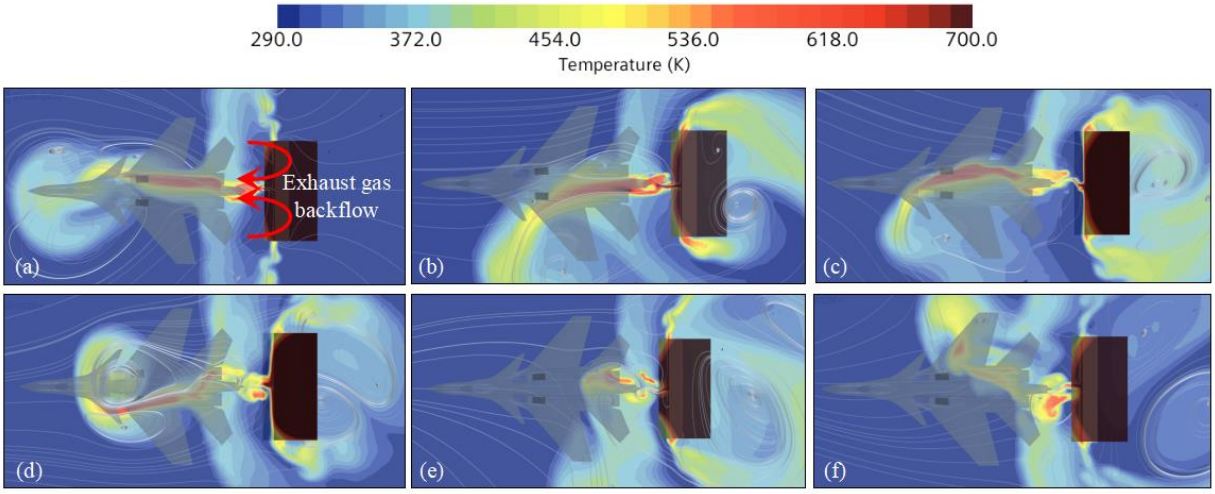


**Figure 10. Exhaust temperature field and streamlines at a plane located 1.0 m above the deck under different wind direction: (a)no wind, (b)headwind, (c)left 22.5°, (d)right 22.5°, (e)left 45°, (f)right 45°**

Fig. 11 illustrates the time-resolved total temperature distortion defined by Eq.(11) under different wind direction conditions. It can be observed that under no-wind condition, the engine begins

to intake high-temperature gas as early as 0.4 seconds, with the fastest temperature rise rate at the AIP. Under headwind or other angled wind conditions, high-temperature gas is not ingested until 0.75 to 1 second. This indicates that during carrier navigation, airflow reduces the accumulation and backflow of hot jet exhaust beneath the fuselage. During the intake process, the total temperature distortion fluctuates due to uneven distribution of hot gas, which is clumped because of the turbulence characteristics and external flow field. When high-temperature gas is ingested by the high-suction engines, surrounding air rushes in to fill the void, leading to temperature fluctuations. The asymmetry of the carrier's structure further complicates the airflow, with recirculation zones formed around the island and deck edges, leading to accumulation of hot exhaust beneath the fuselage. For wind angles of 22.5° or less, at least one engine AIP experiences total temperature distortion exceeding 0.3. Under a right wind 22.5°, the intake temperature distortion is higher on the windward side. When the wind direction increases to 45°, the hot gas is blown out of the accumulation zone. Only a small amount of hot exhaust is ingested into the intakes.

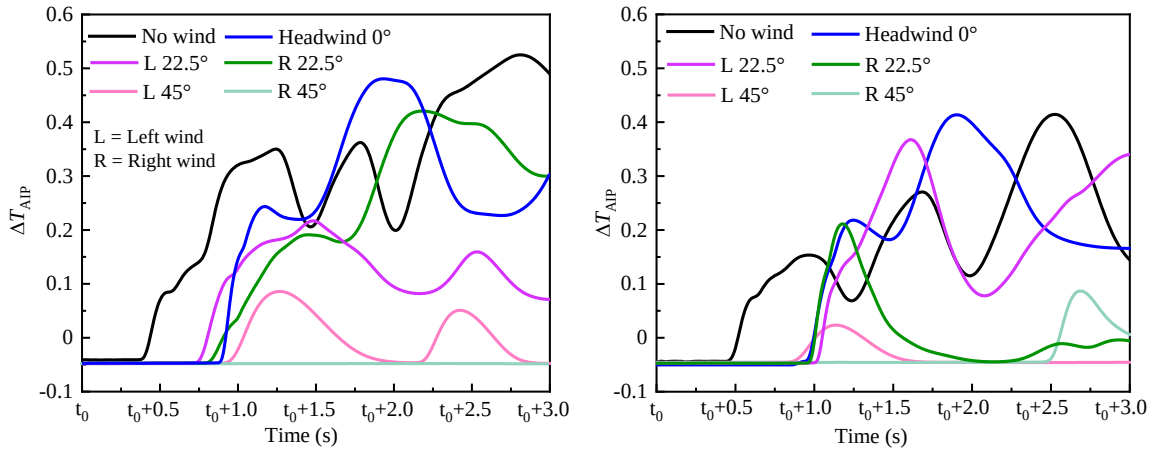


(a) Left engine (b) Right engine

**Figure 11. Temperature distortion under different wind direction**

Fig. 12 presents both the average and maximum temperature distortion values, statistically derived from the data in Fig. 11. The results indicate that under no wind or headwind conditions, the average temperature distortion on both sides of the engine exhibits minimal difference. When the wind direction angle increases to 22.5°, the difference in average temperature distortion between the two sides of the engine becomes significant, leading to a greater disparity in the service life of the engines. At a wind direction angle of 45°, the upwind intake ingests more exhaust gas due to the influence of the swirling flow region above the deck. The engine is most likely to face potential hazards when the temperature distortion reaches its peak. The higher maximum values from Fig. 11(a) or (b) were selected as the basis for comparison. The figure shows that as the wind direction angle increases, both the average and maximum temperature distortion decrease.

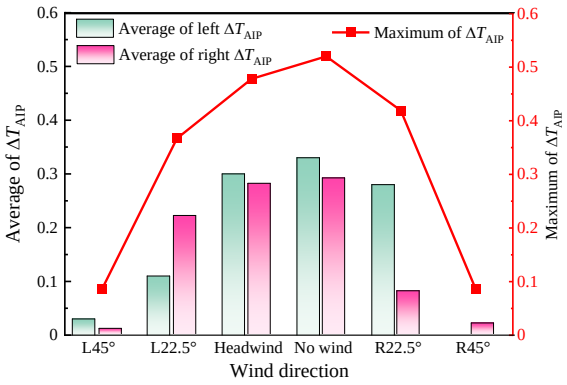


**Figure 12. Temperature distortion under different wind direction**

Fig. 13 shows the dynamic variation of total pressure distortion under different wind direction angles. In this study, the primary cause of total pressure distortion is the geometry of the air inlet duct structure. Affected by the external flow field environment, the total pressure distortion fluctuates within a certain range. As illustrated in the figure, under no-wind condition, the initial total pressure distortion is minimum, and remains relatively stable before high-temperature exhaust is ingested.

In contrast, under windy conditions, the total pressure distortion is higher during the initial stage. After the engines begin to ingest exhaust gas, noticeable fluctuations in total pressure distortion occur under all conditions. This is because the ingestion of high-temperature gas causes rapid changes in airflow velocity, density, and pressure distribution at the AIP. The alternating intake of high- and low-temperature gas further amplifies the fluctuations in total pressure distortion. These fluctuations contribute to flow instability over compressor components and reduce the engine's stability margin.

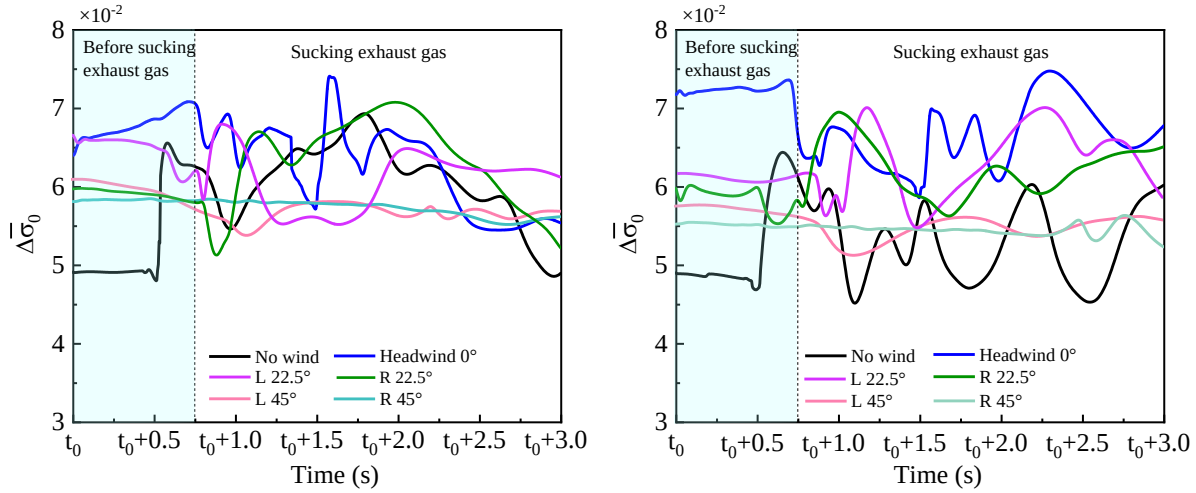


(a) Left engine (b) Right engine

**Figure 13. Total pressure distortion under different wind direction**

Fig. 14 presents a quantitative analysis of total pressure distortion fluctuations using standard deviation. Before the engine ingests hot exhaust gas, minor fluctuations in total pressure distortion are caused by airflow disturbances and the ship's structural impact on the incoming flow. Under no-wind condition or when the wind direction angle is no greater than 22.5°, the ingestion of hot exhaust gas increases the standard deviation by nearly an order of magnitude compared to pre-ingestion levels. The analysis reveals that windless condition is the most challenging for engine intake during the carrier-based aircraft's takeoff phase. When the wind angle is within 22.5°, at least one intake is within the influence zone of high-temperature exhaust, leading to fluctuations in total pressure distortion. Under a large wind angle of 45°, the engine ingests only a small amount of hot gas, with slightly increased fluctuations. However, large wind angles can also

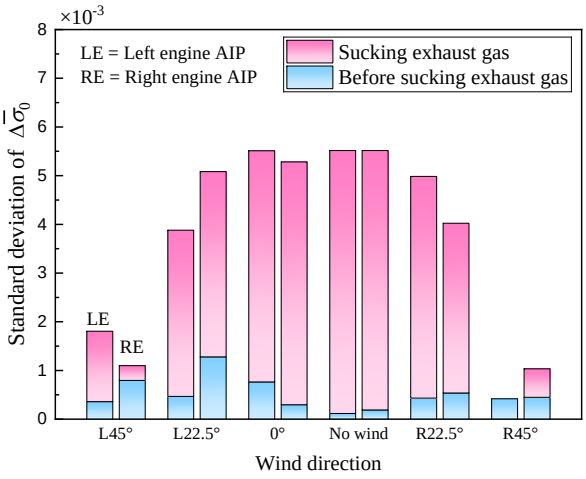


**Figure 14. Standard deviation of total pressure distortion under different wind direction**

affect the stability of the flight system, so the impact of wind angle during carrier-based aircraft takeoff must be considered holistically.

## 4. Conclusion

In this study, the DDES turbulence model was employed to simulate the backflow and ingestion of a carrier-based aircraft engine exhaust under airwake induced by carrier during the takeoff phase. A comparison between nozzle numerical results and experimental data verified the accuracy of the DDES model in predicting high-speed jet impacting on the deflector. The model captured the chaotic, clumped flow features. The major conclusions are summarized as follows:

(1) Exhaust gas is primarily ingested through the auxiliary intake grilles at the bottom of the intake. A strong negative correlation is observed between temperature distortion and the intake flow rate and oxygen content, while a strong positive correlation is found with $CO_2$ and $H_2O$ concentrations. The temperature distortion and total pressure distortion fluctuations exhibit a high degree of synergy. Under headwind condition, the temperature distortion reaches a maximum of 0.49, with intake flow rate decreasing by 23.1% and oxygen content by 8.6%. These factors negatively affect engine stability.

(2) During takeoff on an aircraft carrier deck, recirculation regions at the takeoff position form between the island structure and the inner side of the deck. The exhaust backflow accumulates at the aircraft takeoff position under the influence of recirculation. As the wind angle increases, both the average temperature distortion and the maximum temperature distortion decrease. A quantitative analysis was conducted on the transient correlation between total temperature distortion and total pressure distortion. Standard deviation analysis reveals that larger temperature distortion leads to greater fluctuations in the total pressure distortion index.

## Nomenclature

| | | | |
|---|---|---|---|
| $a$ | the length of the deflector, [m] | $l_2$ | the length of the auxiliary intake grille, [m] |
| $b$ | the width of the deflector, [m] | $\bar{r}$ | the ratio of the radial position to the rim radius at AIP, [-] |
| $D_{\text{in}}$ | the engine inlet diameter, [m] | $t_0$ | the engine activation time, [s] |
| $D_{\text{out}}$ | the engine outlet diameter, [m] | $\Delta T_{\text{AIP}}$ | total temperature distortion, [-] |
| $D_1$ | the experimental nozzle outlet diameter, [m] | ***Greek symbols*** | |
| $h_A$ | the height of the auxiliary intake grille from the deck, [m] | $\gamma$ | the tilt angle of deflector, [°] |
| $h_l$ | the height of the probe line from the deck, [m] | $\delta$ | the distance between AIP and engine inlet, [m] |
| $h_s$ | the height of the horizontal section from the deck, [m] | $\theta$ | the central angle at AIP, [rad] |
| $L$ | the distance between the probe line and the bottom of JBD, [m] | $\sigma_{\text{TPR}}$ | total pressure recovery coefficient, [-] |
| $l$ | the horizontal distance between the engine outlet and the bottom of JBD, [m] | $\Delta\bar{\sigma}_0$ | circumferential distortion index, [-] |
| $l_1$ | the length of the air inlet duct main body, [m] | $\sigma_{\text{av}}$ | average total pressure recovery coefficient, [-] |

**References**


[1] Yue, K., *et al.*, Analysis of Jet Blast Impact of Embarked Aircraft on Deck Takeoff Zone, *Aerospace Science and Technology*, *45* (2015), pp. 60-66

[2] Ma, S., *et al.*, The Effect Analysis of an engine jet on an aircraft blast deflector, *Transactions of the Institute of Measurement and Control*, *41* (2018), 4, pp. 990-1001

[3] Doll, U., *et al.*, Non-Intrusive Flow Diagnostics for Unsteady Inlet Flow Distortion Measurements in Novel Aircraft Architectures, *Progress in Aerospace Sciences*, *130* (2022), 100810

[4] Ozsen, M., and Yildiz, S., Numerical performance analysis of delta vortex generator located upstream of in-line tube bundle, *Thermal Science*, *28* (2024), 4 Part A, pp. 2891-2903

[5] Tanguy, G., *et al.*, Characteristics of Unsteady Total Pressure Distortion for a Complex Aero-Engine Intake Duct, *Aerospace Science and Technology*, *78* (2018), pp. 297-311

[6] Worden, T.J., *et al.*, Supersonic Jet Impingement on a Model-Scale Jet Blast Deflector, *AIAA Journal*, *55* (2017), 8, pp. 2522-2536

[7] Pan, T., *et al.*, Impact of circumferential inlet distortion on different types of stall inceptions in a transonic compressor, *Chinese Journal of Aeronautics*, *37* (2024), 11, pp. 107-117

[8] Zhang, W., *et al.*, Influence of the Inlet Distortion on Fan Stall Margin at Different Rotational Speeds, *Aerospace Science and Technology*, *98* (2020), 105668

[9] Fu, Z., *et al.*, Effects of different oil return pipe locations on the vortex characteristics of a cylindrical cyclone separator, *Thermal Science*, *28* (2024), 3 Part B, pp. 2595-2604

[10] Spasic, Z., *et al.*, Aerodynamic performance of the reversible axial fan for high air temperatures, *Thermal Science*, *27* (2023), 6 Part B, pp. 5053-5062

[11] Zhang, W., and Vahdati, M., A Parametric Study of the Effects of Inlet Distortion on Fan Aerodynamic Stability, *Journal of Turbomachinery*, *141* (2019), 1, 011011

[12] Coschignano, A., and Babinsky, H., Boundary-Layer Development Downstream of Normal Shock in Transonic Intakes at Incidence, *AIAA Journal*, *57* (2019), 12, pp. 5241-5251

[13] Zhang, H., *et al.*, Mechanism of Affecting the Performance and Stability of an Axial Flow Compressor with Inlet Distortion, *Journal of Thermal Science*, *30* (2021), 4, pp. 1406-1420

[14] Vagnoli, S., and Verstraete, T., URANS Analysis of the Effect of Realistic Inlet Distortions on the Stall Inception of a Centrifugal Compressor, *Computers & Fluids*, *116* (2015), pp. 192-204

[15] Rademakers, P.M., *et al.*, Effects of Flow Distortions as They Occur in S-Duct Inlets on the Performance and Stability of a Jet Engine, *Journal of Engineering for Gas Turbines and Power*, *138* (2015), 2, 022605

[16] Triantafyllou, T., *et al.*, Total Pressure Distortion Levels at the Aerodynamic Interface Plane of a Military Aircraft, *The Aeronautical Journal*, *119* (2015), pp. 1147-1166

[17] Alejandro, P., and Hall, A., Aerodynamics of Boundary Layer Ingesting Fuselage Fans, *Journal of Turbomachinery*, *143* (2021), 4, 041007

[18] Cousins, W., History, Philosophy, Physics, and Future Directions of Aircraft Propulsion System/Inlet Integration. Vienna, Austria: ASME Turbo Expo: Turbine Technical Conference and Exposition. Vienna, Austria, 2004.

[19] Xi, L., *et al.*, Study on flow and heat transfer performance of single jet impingement cooling through variable-diameter hole, *Thermal Science*, *28* (2024), 6 Part A, pp. 4499-4517

[20] Li, S., *et al.*, Fluid-thermal-structural coupled investigation on rudder leading edge with porous opposing jet in high-speed flow, *Aerospace Science and Technology*, *155* (2024), pp. 109725-109738

[21] Shin, H.-W., *et al.*, A numerical investigation on the nominal wake of KVLCC2 model ship in regular head waves, *International Journal of Naval Architecture and Ocean Engineering*, *12* (2020), pp. 270-282

[22] Nisham, A., *et al.*, Prediction of the Aerodynamic Behaviour of a Full-Scale Naval Ship in Head Waves Using Detached Eddy Simulation, *Ocean Engineering*, *222* (2021), 108583

[23] Praveen, B., *et al.*, Flow characteristics on helodeck of a generic frigate ship model through experiment and CFD, *Ocean Engineering*, *250* (2022), 110912

[24] Linton, D., and Thornber, B., Quantifying Uncertainty in Turbulence Resolving Ship Airwake Simulations, *Ocean Engineering*, *229* (2021), 108983

[25] Li, T., *et al.*, Numerical study of the flow over the modified simple frigate shape, *Proceedings of the Institution of Mechanical Engineers, Part G: Journal of Aerospace Engineering*, *235* (2020), 12, pp. 1551-1565

[26] Yang, X., *et al.*, Numerical Simulation of the Unsteady Airwake of the Liaoning Carrier Based on the DDES Model Coupled with Overset Grid, *Journal of Marine Science and Engineering*, *12* (2024), 9, pp. 1598-1616

[27] Zhang, J., *et al.*, Comparison of PANS and LES of the Flow Past a Generic Ship, *Ocean Engineering*, *165* (2018), pp. 221-236

[28] Watson, N.A., *et al.*, Computational and Experimental Modelling Study of the Unsteady Airflow over the Aircraft Carrier HMS Queen Elizabeth, *Ocean Engineering*, *172* (2019), pp. 562-574

[29] Shukla, S., *et al.*, Experimental and computational investigation of airwake aerodynamics of the generic aircraft carrier with ski-jump, *Ocean Engineering*, *249* (2022), 110902

[30] Forrest, J.S., and Owen, I., An Investigation of Ship Airwakes Using Detached-Eddy Simulation, *Computers & Fluids*, *39* (2010), 4, pp. 656-673

[31] Shukla, S., *et al.*, Comparative Assessment of URANS, SAS and DES Turbulence Modeling in the Predictions of Massively Separated Ship Airwake Characteristics, *Ocean Engineering*, *229* (2021), 108954

[32] Zamiri, A., and Chung, T., Numerical Evaluation of Wind Direction Effects on the Turbulence Aerodynamics of a Ship Airwake, *Ocean Engineering*, *284* (2023), 115104

[33] Wang, H., *et al.*, Numerical Investigation of Inlet Distortion in a Jet Engine Coupled with Ski-Jump of Carrier-Based Aircraft, *Thermal Science and Engineering Progress*, *43* (2023), 101961

[34] Spalart, P.R., *et al.*, A New Version of Detached-Eddy Simulation, Resistant to Ambiguous Grid Densities, *Theoretical and Computational Fluid Dynamics*, *20* (2006), 3, pp. 181-195

[35] Menter, F.R., *et al.*, Ten years of industrial experience with the SST turbulence model, *Turbulence, Heat and Mass Transfer*, *4* (2003), pp. 625–632

[36] Zhang, Z., *et al.*, Numerical and Test Investigation on an Aircraft Inlet Distortion, *International Journal of Turbo & Jet-Engines*, *30* (2013), 3, pp. 231-241

[37] Henderson, B., *et al.*, An Experimental Study of The Oscillatory Flow Structure of Tone-Producing Supersonic Impinging Jets, *Journal of Fluid Mechanics*, *542* (2005), pp. 115-137

Received: 22.02.2025.
Revised: 16.10.2025.
Accepted: 17.10.2025.